Phys. Status Solidi A **207**, No. 4, 935–942 (2010) / **DOI** 10.1002/pssa.200925579

physica status solidi a
www.pss-a.com
applications and materials science

Editor's Choice

Plasmonic resonances in nanostructured gold/polymer surfaces by colloidal lithography

Silvia Giudicatti[1], Andrea Valsesia[2], Franco Marabelli[*,1], Pascal Colpo[3], and François Rossi[3]

[1] Dipartimento di Fisica 'A. Volta', Università degli Studi di Pavia, via Bassi 6, 27100 Pavia, Italy
[2] Plasmore S.r.l., Via Deledda 4,21020 Ranco (Varese), Italy
[3] Institute for Health and Consumer Protection, Joint Research Centre of the European Commission, via Fermi 1, 21020 Ispra (Varese), Italy

Received 10 November 2009, revised 12 January 2010, accepted 13 January 2010
Published online 1 March 2010

Keywords plasmons, optical properties, nanostructured surfaces, lithography

[*] Corresponding author: e-mail franco.marabelli@unipv.it, Phone: +39 0382 987 709, Fax: +39 0382 987 563

We investigate nanostructured surfaces consisting of a hexagonal lattice of polymeric pillars embedded in a gold matrix. These systems are prepared by a new fabrication technique based on plasma assisted deposition and colloidal lithography. A complete characterization of such surfaces is performed by angle resolved reflectance and transmittance measurements. Both delocalized and localized plasmonic modes can be identified: their reciprocal interplay allows to observe spectral features and to detect refractive index changes related to one of the sample interfaces by measurements performed with a light beam incident from the opposite side. This intriguing behaviour, together with ease of use and low cost of the deposition procedure, make this kind of nanostructures particularly interesting in biosensing applications.

1 Introduction In recent years, a large number of studies on the interaction of electromagnetic waves with nanostructured metallic surfaces has been reported in the literature. In particular, an unexpected enhancement of the transmitted signal through subwavelength holes arrays in metallic films has generated considerable interest due to its numerous potential applications, for example in the field of biodetection.

In 1998, Ebbesen et al. [1] observed for the first time an unusually high optical transmission through a metal film perforated with an array of subwavelength holes. The transmittance spectra have been explained in terms of Wood's anomalies and surface plasmon resonances [2]. Actually, different physical effects and their reciprocal interplay contribute to determine the extremely wide range of observed features. Even the separation between localized and delocalized modes can be questioned in some cases [3]. Isolated nanoholes in optically thick metal films exhibit a distinct optical behaviour in comparison with nanoholes arrays. The transmission properties of isolated subwavelength holes have been investigated both experimentally [4] and theoretically [5, 6]: the excitation of localized surface plasmon (LSP) modes and the coupling of the incident light to waveguide modes inside the hole give rise to enhanced transmission peaks not predicted by Bethe's theory [7]. On the other hand, when the apertures are arranged in a periodic array, nanoholes LSP resonances are expected to couple not only to incident light, but also to surface plasmon polaritons (SPPs) propagating at the metallic interfaces. The interplay between SPP and LSP modes and between SPPs propagating in different directions gives rise to anticrossing and hybridization effects [8, 9].

Ebbesen et al. experimentally investigated the dependence of the transmission on the geometry and the lattice constant of the holes array, the holes size, the film thickness, the refractive index of the dielectric media adjacent to the metal film, the polarization and the direction of the incident light [1, 10–13]. Van der Molen et al. [14] also analysed the role of holes shape and localized resonances in the enhancement of the transmission. On the theoretical side, many papers present analytical studies of the enhanced optical transmission through periodically nanostructured metal interfaces [11, 14–18]; the transmittance enhancement and its dependence on structural parameters have also been

confirmed by numerical simulations: most of them are based on the three-dimensional finite-difference time-domain (3D-FDTD) method [19].

Reflection has not been investigated as widely as transmission. Experimental studies show a significant difference between the reflection spectra for light beams coming from the air side or the substrate of the device [13, 20]. Some theoretical investigations of light reflection from a metal surface with subwavelength apertures have also been proposed [21, 22].

Garcia de Abajo [23] presents an overview of the existing results dealing with the interaction of light with 2D periodic arrays of particles and holes.

Most of the discussed transmittance and reflectance measurements were performed on rectangular or square arrays of subwavelength holes milled through an optically thick metal film by electron- or ion-beam lithography. A different kind of device was investigated by Teperik et al.: they studied both experimentally and theoretically surface and localized plasmons of a hexagonal lattice of spherical nanocavities in a gold film prepared by electrochemical deposition through a self-assembled template [24, 25]. The transition from LSP resonances to delocalized SPPs was also analysed by Murray et al. [26] in silver nanostructures obtained by nanosphere lithography: increasing the etching time, nanoparticles increase in size and merge to create a continuous metallic network perforated by holes.

In the present work, we investigated a series of samples obtained by a new deposition procedure based on colloidal lithography. They consist of a 2D triangular array of plasma polymerized poly-acrylic acid (ppAA) pillars embedded in an optically thick gold film on a glass substrate. Pillars size is large enough to be comparable to both lattice constant and light wavelength in the investigated spectral range. Transmittance and reflectance spectra were acquired by TE and TM polarized light incident from either the air or the glass sides to characterize the optical response of the samples along the main symmetry directions of pillars alignment in the hexagonal structure. We also demonstrated that reflectance measured from one side of the sample is sensitive to a refractive index change at the opposite film interface even if the gold film is relatively thick.

2 Experimental Nanostructured polymer/gold surfaces were prepared using colloidal lithography and plasma enhanced chemical vapour deposition (PE-CVD). A plasma ppAA film was deposited on a glass substrate by PE-CVD using acrylic acid (purity > 99%; Sigma–Aldrich) as liquid precursor. The capacitive coupled plasma source operated at a pressure of 7.5 Pa with a constant monomer flow. The power for plasma generation was provided by a pulsed RF power supply operating at 13.56 MHz and 50 W. Spin coating was then used to cover the film with a monolayer of polystyrene (PS) nanospheres arranged in a 2D hexagonal close-packed lattice. PS beads (Sigma–Aldrich) have a diameter of 500 nm with a nominal size dispersion of 10%.

In order to transfer the geometry of the mask to the underneath layer, the sample was exposed to oxygen plasma etching in a magnetic pole enhanced-ICP source with inductive power $P = 150$ W and DC bias $|V| = 100$ V; the etching time was calculated in order to completely remove the uncovered ppAA areas, while nanoparticles diameter was reduced (in this way, no continuous ppAA film remains on the substrate, but an ordered array of ppAA pillars). A gold layer was then deposited on the sample by physical vapour deposition. Finally, the residual colloidal mask was removed using lift-off by an ultrasonic bath in ultra-pure water.

The resulting structure is a gold film perforated by polymeric pillars arranged in a 2D hexagonal array with lattice constant of 500 nm. The combined control of deposition and etching parameters allows the tuning of film thickness and pillars diameters. Investigated samples have a nominal thickness of 140 nm and polymeric pillars top diameter of about 150 nm. Samples were characterized by atomic force microscopy (AFM). Figure 1a shows an AFM image of a region of the sample surface, while Fig. 1b reports the AFM surface profiles acquired before (solid line) and after (dashed line) gold deposition (a portion of the sample was detached and lift-off before gold deposition): we can

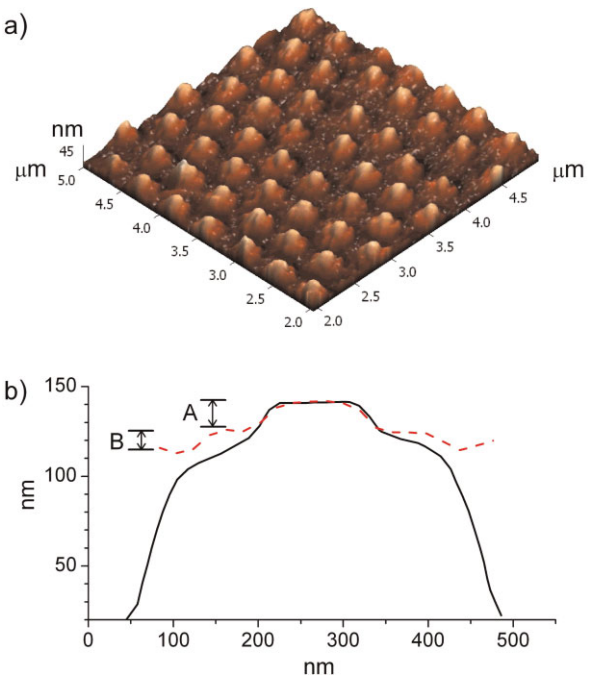

Figure 1 (online colour at: www.pss-a.com) (a) AFM image of a sample surface region. (b) AFM surface profiles acquired before (solid line) and after (dashed line) gold deposition (a portion of the sample was detached and lift-off before gold deposition). The solid line represents the cross-section of the pillar, whereas the dashed line is the surface profile of the finished sample. The two lines have been aligned to the top of the pillar, which was under the PS mask. The space between them is filled by gold. Pillar top emerges 10–20 nm from gold (step A) and the step B corresponds to a gold ring around the polymeric pillar.

notice that polymeric structures emerge 10–20 nm above the metallic layer. A SEM image of a typical sample surface is presented in Fig. 2: it is evident that the sample surface is not flat, but 10 nm high gold rings surround the emerging ppAA pillars (appearing dark); a residual PS sphere is also visible.

The optical characterization of the samples was carried out by angle-resolved reflection and transmission measurements over the spectral range 9000–25 000 cm^{-1}. A home made microreflectometer setup associated with a commercial FT spectrometer was used to investigate the sample surface with a light spot having diameter of 100 μm and divergence less than 2°. For the dispersion measurements, the angle of incidence θ was varied between 0° (5° for reflectance) and 55°. The reflected beam was collected at 2θ by a silicon photodiode. A Glan Taylor polarizer was used to select TE or TM polarized light (electric- or magnetic-field perpendicular to the incidence plane, respectively). Since lattice geometry also affects the behaviour of SPPs, it is important to verify that the light spot is covering a homogeneously oriented domain of the sample surface: a camera was used to locate the most uniform surface areas.

In order to analyse the effect of a refractive index change at the free interface of the device, reflectance measurements at fixed incidence angle (5°) were performed by TM polarized light incident from the substrate while different aqueous solutions flow on the exposed surface by means of a home made flow cell connected with a peristaltic pump.

3 Results Figure 3a reports the reflectance spectra acquired with TM polarized light from the air side of the sample for different incidence angles and with the plane of incidence perpendicular to the pillars lines; we use this orientation as a reference, $\Phi = 0°$. At near normal incidence (5°), reflectance exhibits two main minima located at about 11 500 and 14 500 cm^{-1}, followed by a monotonic decrease for increasing wavenumbers above 16 000 cm^{-1}. For larger incidence angles, a progressive red shift of minima appears together with a splitting of such structures: at least four small minima can be noticed for angles larger than 15°. The energies of reflectance minima for incidence angles $\theta = 5°$ and 50° are indicated by vertical bars in Fig. 3a. TE reflectance behaviour (Fig. 3b) is qualitatively similar to TM response but for the much lower intensity and dispersion of the spectral features at the highest frequencies.

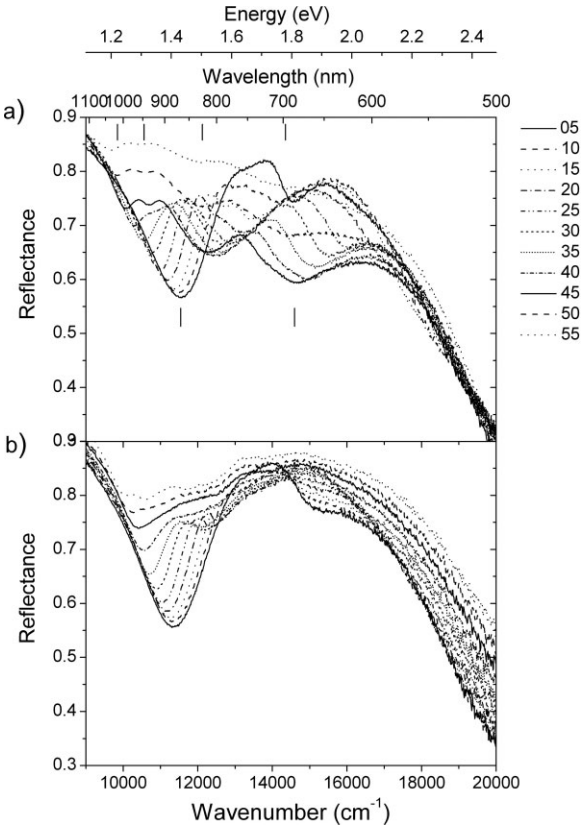

Figure 3 Reflectance spectra measured from the air side of the sample with azimuthal orientation $\Phi = 0°$ by TM (a) and TE (b) polarized light for different incidence angles ($5° < \theta < 55°$). Vertical marks in section (a) indicate the energies of the reflectance minima for $\theta = 5°$ (below) and $\theta = 50°$ (above).

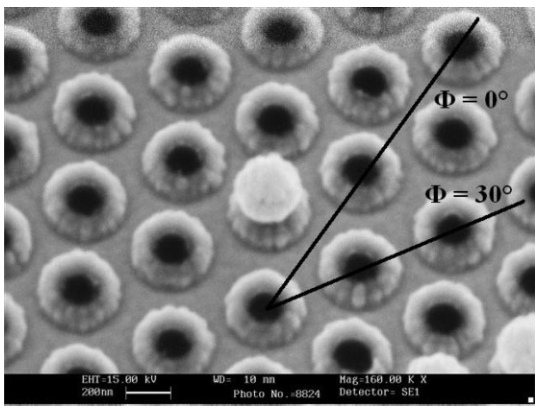

Figure 2 SEM image of a sample surface region after the lift-off process. The top of the ppAA pillars appears black in the image; a residual PS nanosphere is also visible. Black lines indicate the symmetry lines corresponding to azimuthal angles $\Phi = 0°$ and 30°, along which the plane of incidence was aligned for reflectance measurements.

A rotation of the sample around the normal to the surface by an angle Φ causes a change of the alignment of the incidence plane with respect to the pillars lines and introduces a slight shift of the reflectance features. As a matter of fact, due to the sixfold symmetry of the 2D pillars array, such a shift is recovered every 60°. In the dispersion diagrams of Fig. 4, the intensity of the second derivative of the reflectance spectra is displayed as a function of wavenumbers and incidence angle: minima of reflectance correspond to maxima in second derivative. Figure 4a and b are related to the reflectance measured with TM polarized light incident from the air side of the sample for azimuthal orientations of the incidence plane $\Phi = 0°$ and 30°, respectively. At near normal incidence, when the azimuthal

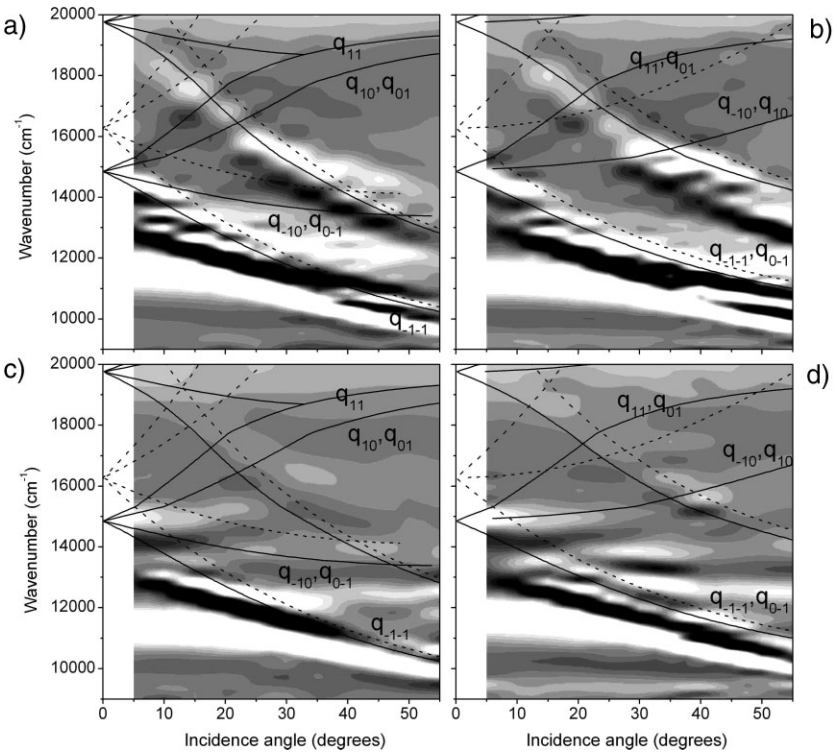

Figure 4 Intensity of second derivative of reflectance spectra as a function of wavenumbers and incidence angle. Reflectance was measured by TM (a, b) and TE (c, d) polarized light from the air side of the sample for azimuthal orientations $\Phi = 0^\circ$ (left) and 30° (right). Grey scale is dark for lower intensities and white for higher intensities. Calculated energy dispersions of SPPs (solid lines) and Wood's anomalies (dashed lines) at the air and glass sides (upper and lower groups, respectively) are superimposed on experimental data. Calculated curves related to the gold/glass interface are labelled by the reciprocal lattice vectors $\boldsymbol{q}_{nm}$.

angle Φ changes from 0° to 30°, the reflectance dip located between 11 000 and 12 000 cm^{-1} slightly red-shifts, whereas the plasmonic mode in the spectral range 14 000–15 000 cm^{-1} moves to higher wavenumbers. For symmetry reasons, the reverse occurs for TE polarization. Results obtained with TE polarization for $\Phi = 0^\circ$ and 30° are shown in Fig. 4c and d, respectively. In the measured spectral range, there is a dominant reflectance dip which moves from 12 000 to 10 000 cm^{-1} when the angle of incidence increases. Besides this structure, nearly dispersionless resonances can be seen. The dispersion diagrams show a reflectance minimum at 15 000 cm^{-1} when the angle of incidence is less than 20° and a resonance located between 12 000 and 13 000 cm^{-1} at angles of incidence greater than 35°. A comparison between Fig. 4c and d indicates that a change in the azimuthal angle affects the spectral position of the reflectance minima.

Figure 5 reports the reflectance spectra acquired by TM polarized light incident from the substrate for azimuthal orientation $\Phi = 0^\circ$. The optical response is quite similar to that observed for TM polarized light incident from the air side, in particular because of the dispersive behaviour at the largest incidence angles and below 13 000 cm^{-1}. The main difference consists in the presence of a reflectance minimum which moves from 15 000 to 16 000 cm^{-1} for angles increasing from 5° to 25°. Instead, the spectral minimum above 17 000 cm^{-1} observed in Fig. 4a is not noticeable here. One can also notice that the reflectance minimum at about 14 500 cm^{-1} for $\theta < 25^\circ$ in Fig. 4a closely corresponds to a pronounced reflectance peak in Fig. 5b.

The transmittance data (TM polarization, $\Phi = 0^\circ$) are presented in Fig. 6. Please note that the grey scale has been reversed with respect to the previous diagrams in order to put transmittance maxima in correspondence with reflectance minima (and *vice versa*). Let us also notice that it has been possible to obtain transmittance data at normal incidence. The results exhibit a close correspondence with the reflectance spectra; in particular, the evident transmittance maximum which moves from 11 500 to 10 000 cm^{-1} is clearly related to the reflectance minimum observed in Fig. 4a.

Figure 7a compares reflectance spectra measured by TM polarized light for 5° incidence angle when the free surface of the device is exposed inside a flow cell to air and to a phosphate-buffered saline (PBS) solution. Let us notice that the pronounced reflectance minimum at about 11 000 cm^{-1} is red-shifted with respect to the previously shown results since, in this case, the pillars size is slightly larger than in the sample related to the experimental data discussed above. Further measurements performed on several slightly different samples show a clear correlation between the pillars radius (tuned by the etching time) and the spectral position of the dispersionless resonances, whereas no similar dependence seems to affect the dispersive modes. The refractive index change at the exposed surface clearly affects the spectral position and line width of the main reflectance features: the ratio between reflectance spectra measured with and without PBS inside the flow cell (Fig. 7b) shows a relative signal change reaching 100% in correspondence with the pronounced reflectance minimum around 11 000 cm^{-1}.

When PBS replaces air, the refractive index change is large; in order to estimate our systems sensitivity, we measured the same ratio for reflectance spectra acquired while salt solutions with different concentration (and, consequently, with different refractive index) flow inside the cell. Figure 8 shows the response of the device to distilled water and a salt solution with concentration 1%: a refractive index variation of 0.0018 (www.topac.com/

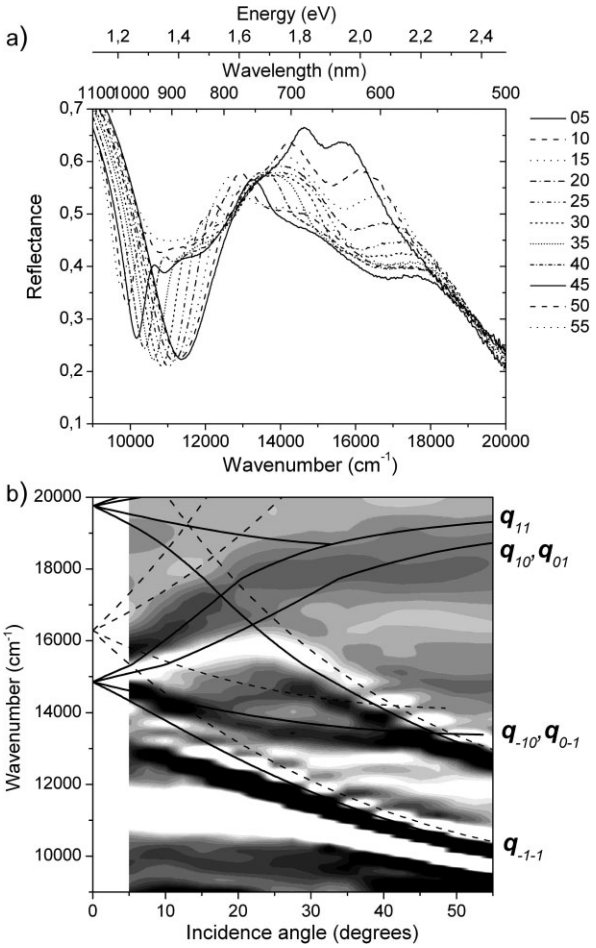

Figure 5 Reflectance measured by TM polarized light from the glass side of the sample for azimuthal orientation $\Phi = 0^\circ$. (a) Reflectance spectra for different incidence angles ($5^\circ < \theta < 55^\circ$). (b) Intensity of second derivative of reflectance spectra as a function of wavenumbers and incidence angle. Grey scale is dark for lower intensities and white for higher intensities. Calculated energy dispersions of SPPs (solid lines) and Wood's anomalies (dashed lines) at the air and glass sides (upper and lower groups, respectively) are superimposed on experimental data. Calculated curves related to the gold/glass interface are labelled by the reciprocal lattice vectors $\boldsymbol{q}_{nm}$.

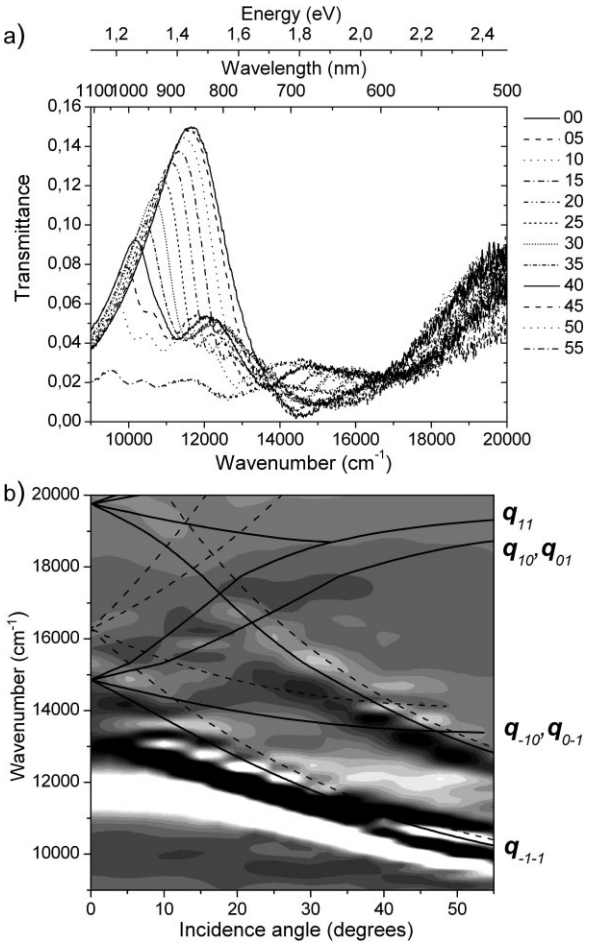

Figure 6 Transmittance measured by TM polarized light for azimuthal orientation $\Phi = 0^\circ$. (a) Transmittance spectra for different incidence angles ($0^\circ < \theta < 55^\circ$). (b) Intensity of second derivative of transmittance spectra as a function of wavenumbers and incidence angle. Grey scale is white for lower intensities and dark for higher intensities. Calculated energy dispersions of SPPs (solid lines) and Wood's anomalies (dashed lines) at the air and glass sides (upper and lower groups, respectively) are superimposed on experimental data. Calculated curves related to the gold/glass interface are labelled by the reciprocal lattice vectors $\boldsymbol{q}_{nm}$.

Salinity_brix.html) determines a relative signal change of several percent.

4 Discussion According to Ghaemi et al. [2], transmittance minima are related to Wood's anomaly, whereas transmittance maxima result from a resonant interaction of the incident light with SPPs on both interfaces of the metal film. Such an interaction is allowed by coupling through the grating momentum [27].

We calculated the energy dispersion of these modes in our case by assuming the investigated nanostructured metallic film as a flat gold surface with a hexagonal lattice of scattering points [25]. The lattice constant is determined by the diameter of the colloidal mask nanospheres. SPPs energies are given by

$$E(\theta, \phi) = \hbar c \sqrt{\frac{\varepsilon_m(E) + \varepsilon_d}{\varepsilon_m(E)\varepsilon_d}} |\boldsymbol{k}_0(\phi) \sin\theta + \boldsymbol{q}_{nm}| \qquad (1)$$

where $\boldsymbol{k}_0 \sin\theta$ is the in-plane wavevector of the incident light and must take into account the lattice orientation (azimuthal angle Φ). $\boldsymbol{q}_{nm}$ are the reciprocal lattice vectors for the hexagonal lattice. ε_d denotes the permittivity of the dielectric medium above gold surface: it is assumed to be equal to 1 and 2.1 at the air and glass sides, respectively.

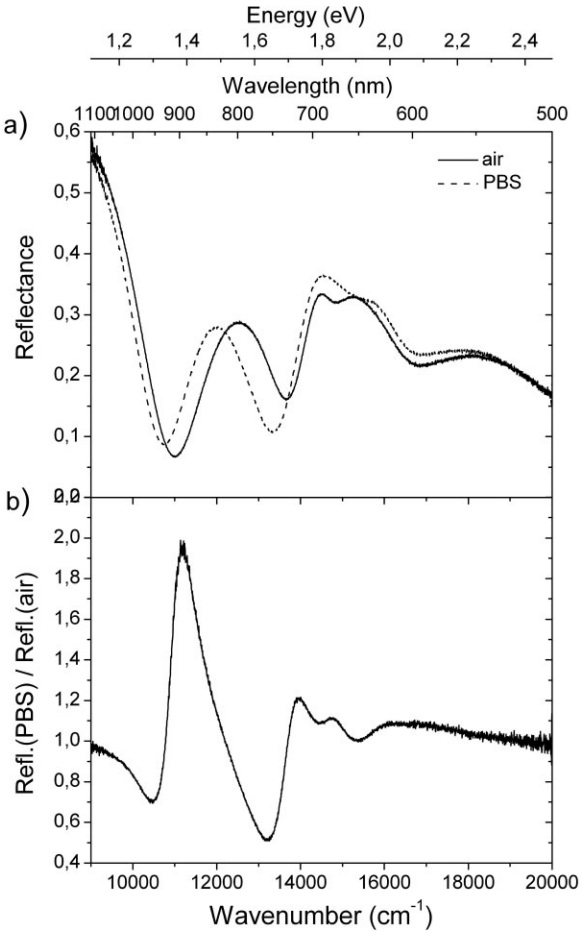

Figure 7 (a) Reflectance measured by TM polarized light for 5° when the flow cell is filled with air or PBS solution ($n \approx 1.33$). (b) Ratio of reflectance measured with PBS inside the cell to reflectance measured when the cell was empty.

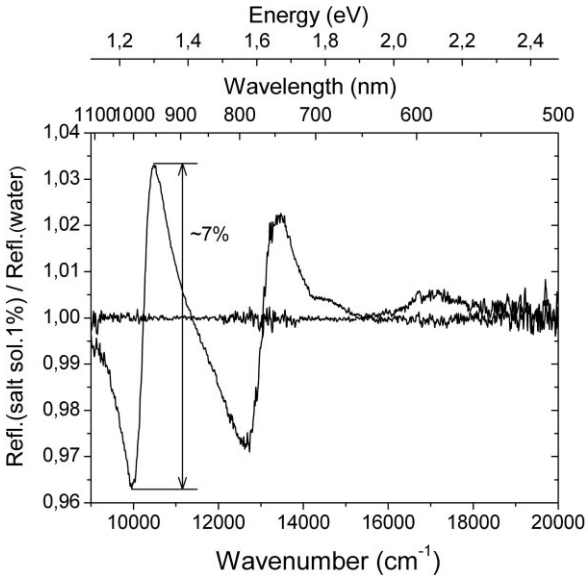

Figure 8 Reflectance measured by TM polarized light for 5° when the flow cell is filled with a salt solution with concentration 1% ($n = 1.3348$). Distilled water ($n = 1.333$) was assumed as reference. The difference between maximum and minimum values reaches 7% in the spectral range 9000–12 000 cm^{-1}.

ε_m indicates the energy-dependent complex permittivity of gold [28]. If only smallest $\boldsymbol{q}_{nm}$ are considered, Eq. (1) has six solutions. However, degeneracies at symmetry orientations $\Phi = 0°$ and 30° reduce their number to four and three, respectively.

Calculated energy dispersions of SPPs (solid lines) and Wood's anomaly (dashed lines) at the air and glass interfaces (upper and lower groups, respectively) are superimposed on the diagram of the measured transmittance (Fig. 6b). There is no evidence for a clear correlation between calculated Wood's modes and transmittance features. The only transmittance minimum which seems to be connected to Wood's anomaly lies in the spectral range 14 000–15 000 cm^{-1} for incident angles between 20° and 40°. On the contrary, some transmittance maxima behaviour is reproduced by calculated SPP dispersions: notice, in particular, $\boldsymbol{q}_{-1\text{-}1}$ mode related to the air side and $\boldsymbol{q}_{-10}$, $\boldsymbol{q}_{0\text{-}1}$ and $\boldsymbol{q}_{-1\text{-}1}$ modes supported by the glass/gold interface. The transmittance response is not well-defined above 16 000 cm^{-1}. We also compared calculated SPP dispersions with reflectance data. In the measured spectral range, the SPP penetration depth into the metal, estimated to be approximately 30 nm, should prevent the direct coupling between surface plasmons supported by the opposite sides of the device. In fact, measuring from the air side, the strong coupling between light and $\boldsymbol{q}_{10}$, $\boldsymbol{q}_{01}$ glass mode is not noticeable (see Fig. 4a), whereas Fig. 5b (glass side reflectance) does not reveal the interaction of light with $\boldsymbol{q}_{-1\text{-}1}$ air mode above 17 000 cm^{-1}. However, in either case, reflectance exhibits together spectral features resulting from the coupling of incident light with SPPs related to both glass ($\boldsymbol{q}_{-1\text{-}1}$) and air ($\boldsymbol{q}_{-1\text{-}1}$ below 17 000 cm^{-1}) sides of the sample.

It is anyway worth to notice that, due to the complex structure of gold surface and ppAA pillars, within the framework of the Ghaemi's interpretation many features in the spectra remain unexplained. In particular, the pronounced spectral structure at about 11 500 cm^{-1} observed in all spectra both in reflectance and in transmittance cannot be explained. Actually, the dependence of such feature energy on the pillars size suggests that charge oscillations localized inside the polymeric nanostructures must also be considered. They both affect polaritons dispersion and strongly support the coupling between SPPs at the opposite film sides.

To give a rough estimate of such resonances, we tried to consider acrylic acid pillars as isolated spherical dielectric cavities completely embedded in an infinite gold matrix [25]. The electromagnetic solutions of such a system correspond to Mie scattered modes from a sphere [29]. These are calculated from Maxwell's equations expanded in spherical

coordinates by requiring boundary conditions at the sphere surface. TM modes energies are given by

$$\varepsilon_m(\omega)h_l(\boldsymbol{k}_mR)[\boldsymbol{k}_dRj_l(\boldsymbol{k}_dR)]\prime + \\ -\varepsilon_d j_l(\boldsymbol{k}_dR)[\boldsymbol{k}_mR\,h_l(\boldsymbol{k}_dR)]\prime = 0 \quad (2)$$

where R corresponds to the sphere radius, $\boldsymbol{k}_d$ and $\boldsymbol{k}_m$ are the wavevectors inside and outside the cavity, respectively. ε_d and ε_m indicate the dielectric constants of the cavity dielectric medium and gold: ε_d is assumed to be frequency-independent and equal to 2.86 (ppAA) [30], while ε_m is calculated by Drude's model. j_l and h_l denote spherical Bessel and Hankel functions of lth order; the prime indicates differentiation with respect to the argument kR. A resonance at about 11 500 cm^{-1} can be obtained for a sphere radius of about 160 nm: this value is in good agreement with real pillars size, as observed in Fig. 1b. In the framework of this model, the next mode lies at about 14 500 cm^{-1}. TE transmittance data (not shown) clearly exhibit a dispersionless maximum at about 14 000 cm^{-1} for $\theta < 30^\circ$. Actually, TE transmittance reveals other nearly dispersionless resonances not predicted by Mie theory, in particular, at about 13 000 cm^{-1} (maximum) for $\theta > 20^\circ$, 14 500 cm^{-1} (minimum) for $\theta < 25^\circ$ and 16 000 cm^{-1} (maximum) for incident angles between 0° and 10°. Some correspondence to these features can be found in TE reflectance data.

Actually, AFM image in Fig. 1b clearly reveals that spheres can only roughly represent our polymeric pillars. Cole et al. [31] have proposed a numerical method to calculate energies and fields of localized modes in truncated spherical nanovoids embedded in a metallic film. According to this method, the presence of the aperture in the cavity breaks the degeneracy with respect to the azimuthal quantum number m: i.e. the l spherical void modes are split into m states, whose energy tuning closely depends on the field distribution of each mode. This splitting can probably explain the extra modes observed experimentally. Moreover, the dependence of their intensity on the incidence angle can also be accounted by the m-dependent electric field orientation.

An alternative approach to describe the optical response of the investigated system consists in considering polymeric pillars as cylindrical cavities. We analysed propagating and surface modes inside a z-invariant dielectric waveguide within an infinite metallic matrix [32]: their energy intrinsically depends on both cylinder radius and field orientation with respect to z-axis. Frequency values compatible with experimental resonances can be obtained from cylinder radii slightly larger (200–220 nm) than in the Mie model. It is interesting to notice that the possibility of energy transfer along the cylinder axis introduces a small wavevector dependence of modes. As a matter of fact, a dispersive behaviour can be observed for the resonance at 11 500 cm^{-1} when incidence angle increases. On the other hand, $\boldsymbol{q}_{\text{-1-1}}$ glass mode and $l = 1$ resonance become degenerate at about 25°, where an anticrossing feature can be recognized. This should imply a mixing of localized and delocalized modes which is highly compatible with the observation of the same resonances on both interfaces. Consequently, dispersion features are introduced for localized modes too. In addition, an intersite interaction of such modes is highly probable because of the large size of the pillars with respect to the lattice constant. Some other spectral features remain to be interpreted. The minimum at about 14 500 cm^{-1} for $\theta = 5^\circ$ in reflectance spectra acquired from the air side, exactly corresponds to a pronounced reflectance peak when the sample is investigated from the glass side. In either case, measured spectral features follow the calculated dispersion of $\boldsymbol{q}_{\text{0-1}}$, $\boldsymbol{q}_{\text{-10}}$ glass mode. Since localized $l = 2$ resonance is not far in energy, this minimum–maximum exchange could be related to field symmetry effects mediated by the localized resonance. Another anomaly consists in the smooth dispersion of the $\boldsymbol{q}_{\text{-1-1}}$ glass mode at the lowest incidence angles. When $\theta = 0^\circ$, the measured spectral feature lies at about 13 500 cm^{-1}: it remains below the calculated SPP crossing point at about 15 000 cm^{-1}. On the other hand, a weak spectral feature related to the $\boldsymbol{q}_{11}$ glass mode can be observed at about 16 000 cm^{-1} both in reflectance and in transmittance. This effect could be ascribed to the strong lattice potential: when $\theta = 0^\circ$, it removes the SPP degeneracy resulting in an energy gap [33, 34].

The main result emerging from the above discussion is that reflectance measured from one side of the sample is sensitive to the refractive index at the opposite film interface even if the gold film is relatively thick. This behaviour is confirmed by the evident shift in energy of the main features of reflectance spectra acquired from the substrate side when the dielectric medium on the exposed surface is changed (Fig. 7a): experimental results show that not only SPPs but also localized plasmonic resonances red shift when PBS replaces air inside the cell. In the air-PBS case, the refractive index change is large. However, the reflectance measurements performed with saline solutions inside the flow cell (Fig. 8) prove that the investigated samples can detect very small refractive index variations. Since a refractive index increase of 0.0018 results in a 7% signal amplitude variation and the noise in the baseline is below 0.2%, we would be able to detect refractive index changes of the order of 10^{-5}.

5 Conclusions In conclusion, the optical characterization of a new class of nanostructured gold surfaces prepared by colloidal lithography on a polymeric film has been presented and discussed. The non-conventional shape of the polymeric nanostructures in the investigated samples makes it difficult to give a definitive assessment to each detail of the wealth of the measured spectral features. Anyway, we have proposed a sketch of involved phenomena and some hints for their interpretation. The strong interplay between plasmonic modes on both sample sides and the simple fabrication technique provide not only an interesting playground to study interaction effects, but also a promising configuration for biosensing applications. Ordered arrays of ppAA nanopillars are demonstrated to improve the bioactivity of

deposited proteins with respect to uniform films, leading to an enhancement in biorecognition [35–37]. The investigated samples are proved to detect refractive index changes at the free surface of the order of 10^{-5}, not far from traditional SPR biosensors sensitivity. An advantage with respect to conventional SPR devices (composed of a thin metallic film) is the possibility of measuring the optical response from the backside of a flat sample without expensive and delicate prism based optics.

Acknowledgements The authors gratefully acknowledge the support of Cariplo Foundation.

References

[1] T. W. Ebbesen, H. J. Lezec, H. F. Ghaemi, T. Thio, and P. A. Wolff, Nature **391**, 667 (1998).
[2] H. F. Ghaemi, T. Thio, D. E. Grupp, T. W. Ebbesen, and H. J. Lezec, Phys. Rev. B **58**, 6779 (1998).
[3] M. I. Stockman, S. V. Faleev, and D. J. Bergman, Phys. Rev. Lett. **87**, 167401 (2001).
[4] A. Degiron, H. J. Lezec, N. Yamamoto, and T. W. Ebbesen, Opt. Commun. **239**, 61 (2004).
[5] E. Popov, N. Bonod, M. Neviere, H. Rigneault, P. F. Lenne, and P. Chaumet, Appl. Opt. **44**, 2332 (2005).
[6] H. Shin, P. B. Catrysse, and S. Fan, Phys. Rev. B **72**, 085436 (2005).
[7] H. A. Bethe, Phys. Rev. **66**, 163 (1944).
[8] C. Sauvan, C. Billaudeau, S. Collin, N. Bardou, F. Pardo, J. L. Pelouard, and P. Lalanne, Appl. Phys. Lett. **92**, 011125 (2008).
[9] J. Li, H. Iu, J. T. K. Wan, and H. C. Ong, Appl. Phys. Lett. **94**, 033101 (2009).
[10] T. Thio, H. F. Ghaemi, H. J. Lezec, P. A. Wolff, and T. W. Ebbesen, J. Opt. Soc. Am. B **16**, 1743 (1999).
[11] A. Krishnan, T. Thio, T. J. Kim, H. J. Lezec, T. W. Ebbesen, P. A. Wolff, J. Pendry, L. Martin-Moreno, and F. J. Garcia-Vidal, Opt. Commun. **200**, 1 (2001).
[12] A. Degiron, H. J. Lezec, W. L. Barnes, and T. W. Ebbesen, Appl. Phys. Lett. **81**, 4327 (2002).
[13] W. L. Barnes, W. A. Murray, J. Dintinger, E. Devaux, and T. W. Ebbesen, Phys. Rev. Lett. **92**, 107401 (2004).
[14] K. L. Van der Molen, K. J. Klein Koerkamp, S. Enoch, F. B. Segerink, N. F. van Hulst, and L. Kuipers, Phys. Rev. B **72**, 045421 (2005).
[15] L. Martin-Moreno, F. J. Garcia-Vidal, H. J. Lezec, K. M. Pellerin, T. Thio, J. B. Pendry, and T. W. Ebbesen, Phys. Rev. Lett. **86**, 1114 (2001).
[16] S. A. Darmanyan and A. V. Zayats, Phys. Rev. B **67**, 035424 (2003).
[17] C. P. Huang, Q. J. Wang, and Y. Y. Zhu, Phys. Rev. B **75**, 245421 (2007).
[18] L. Martin-Moreno and F. J. Garcia-Vidal, J. Phys.: Condens. Matter **20**, 304214 (2008).
[19] Y. Chen, Y. Wang, Y. Zhang, and S. Liu, Opt. Commun. **274**, 236 (2007).
[20] E. Altewischer, M. P. van Exter, and J. P. Woerdman, Opt. Lett. **28**, 1906 (2003).
[21] M. Sarrazin and J. P. Vigneron, Phys. Rev. B **70**, 193409 (2004).
[22] C. P. Huang, J. Q. Li, Q. J. Wang, X. G. Yin, and Y. Y. Zhu, Appl. Phys. Lett. **93**, 081917 (2008).
[23] F. J. Garcia de Abajo, Rev. Mod. Phys. **79**, 1267 (2007).
[24] T. W. Teperik, V. V. Popov, F. J. Garcia de Abajo, T. A. Kelf, Y. Sugawara, J. J. Baumberg, M. Abdelsalam, and P. N. Bartlett, Opt. Express **14**, 11964 (2006).
[25] T. A. Kelf, Y. Sugawara, R. M. Cole, J. J. Baumberg, M. E. Abdelsalam, S. Cintra, S. Mahajan, A. E. Russell, and P. N. Bartlett, Phys. Rev. B **74**, 245415 (2006).
[26] W. A. Murray, S. Astilean, and W. L. Barnes, Phys. Rev. B **69**, 165407 (2004).
[27] H. Raether, Surface Plasmons on Smooth and Rough Surfaces and on Gratings (Springer-Verlag, Berlin/Heidelberg, 1988).
[28] E. D. Palik, Handbook of Optical Constants of Solids, Vol. 1 (Academic Press, New York, 1980), pp. 293–294.
[29] A. Boardman, Electromagnetic Surface Modes (John Wiley and Sons, New York, 1982).
[30] A. Valsesia, Fabrication of Nanostructured Surfaces for the Development of Advanced Biointerfaces, Ph.D. Thesis (University of Pavia, printed in Pavia, Italy, November 2007), ISBN 978-88-95767-12-4.
[31] R. M. Cole, J. J. Baumberg, F. J. Garcia de Abajo, S. Mahajan, M. E. Abdelsalam, and P. N. Bartlett, Nano Lett. **7**, 2094 (2007).
[32] J. D. Jackson, Classical Electrodynamics, 3rd ed. (John Wiley, New York, 1998).
[33] W. L. Barnes, T. W. Preist, S. C. Kitson, and J. R. Sambles, Phys. Rev. B **54**, 6227 (1996).
[34] S. C. Kitson, W. L. Barnes, and J. R. Sambles, Phys. Rev. Lett. **77**, 2670 (1996).
[35] A. Valsesia, P. Colpo, T. Meziani, P. Lisboa, M. Lejeune, and F. Rossi, Langmuir **22**, 1763 (2006).
[36] A. Valsesia, I. Mannelli, P. Colpo, F. Bretagnol, and F. Rossi, Anal. Chem. **80**, 7336 (2008).
[37] S. Mornet, F. Bretagnol, I. Mannelli, A. Valsesia, L. Sirghi, P. Colpo, and F. Rossi, Small **4**, 1919 (2008).

